# Error surface topology in the data analysis of laser-induced thermal acoustics signals

**Journal Article**

**Author(s):**
Schlamp, Stefan; Schmid, Lukas

# Error Surface Topology in the Data Analysis of Laser-Induced Thermal Acoustics Signals

**Stefan Schlamp and Lukas Schmid**

ETH Zürich, Institute of Fluid Dynamics, Sonneggstr. 3, 8092 Zürich, Switzerland

E-mail: `schlamp@ifd.mavt.ethz.ch`

**Abstract.** Laser-induced thermal acoustics (LITA) promises remote, instantaneous and non-intrusive point-measurements of the speed of sound (temperature), thermal diffusivity (density), flow velocity (Mach number), and a species concentration simultaneously in harsh environments. The data analysis relies on a non-linear fit of an analytical model to the acquired data. The measured quantities are parameters in the model. Computational cost and convergence behavior depend on the dimensionality of the parameter space, the initial guesses for the parameters and on whether the data analysis is performed in the time or frequency domain. The topology of the four-dimensional error surface is discussed and a characteristic allowable distance of the initial guesses from the global minimum is defined and quantified for typical configurations. Noise has no significant influence on the convergence neighborhood or the computational cost. If improved initial guesses (10% maximum error) for the speed of sound and the flow velocity are obtained by data preprocessing, convergence of the fitting algorithm is ensured.

PACS numbers: 42.65.-k (Nonlinear optics), 43.58Dj (sound velocity), 06.30.Gv (Velocity, acceleration, and rotation), 07.05Kf (Data analysis: algorithms and implementation; data management)

Submitted to: *Meas. Sci. Technol.*

## 1. Introduction

Laser-induced thermal acoustics (LITA) is a four-wave mixing laser diagnostic point measurement technique that was originally conceived and developed by Cummings at the California Institute of Technology in 1995 for remote, instantaneous, and high-accuracy measurements of the speed of sound and the thermal diffusivity of non-opaque fluids [1–4]. Recent developments additionally permit the measurement of one velocity component in sub- [5–8] and supersonic [9] flows using thermal [8, 10] or electrostrictive [5, 7] gratings as well as, under certain conditions, species concentrations [11]. LITA does not require tracers and is insensitive to flow luminosity. In previous experiments only one or two out of the four parameters (speed of sound, $c_s$, flow velocity, $u_y$, thermal diffusivity, $D_T$, and concentration, $c$) have been measured simultaneously. In principal, all four quantities can be measured simultaneously. Some *a priori* considerations for the data analysis of such measurements are discussed in this paper. An introduction to laser-induced thermal acoustics is given in section 2. Section 3 addresses the special implications for the data analysis when measuring four parameters simultaneously. These implications are quantified in Section 4, where the results of a numerical study are presented and discussed.

## 2. Laser-Induced Thermal Acoustics

Two focused, pulsed laser beams (excitation beams) intersect path-length matched at a shallow angle in the sample volume. A three-dimensional Gaussian-shaped interference grating (half-width in the order of 100 $\mu$m) is created with fringe spacings in the order of a few $\mu$m. Unlike in Laser Doppler Anemometry (LDA), however, the power of the excitation laser is sufficient to inscribe a density perturbation grating into the fluid. One of two (or both) molecular mechanisms are responsible for density changes. Thermalization is the process of energy absorption by fluid molecules and its subsequent conversion into thermal energy by means of inelastic collisions. Electrostriction is the tendency of polarizable molecules to move under the action of a potential field caused by interactions of an optically induced dipole moment and the optical field. Mathematically, while thermalization is treated as a driving term in the energy equation, electrostriction is a driving term in the momentum equation.

In both excitation mechanisms, a pair of acoustic waves is created which travel in opposite directions at the local speed of sound relative to the surrounding fluid. In the case of thermalization, a stationary thermal density grating is also created which decays due to thermal diffusion. At $t = 0$ (the time of the excitation laser pulse which is assumed to be a Delta-function in time) the various density gratings cancel but for $t > 0$ they interfere constructively and destructively with each other so that a net density grating exists in the sample volume. The evolution of the density grating can be observed by a cw laser (interrogation laser) directed at the Bragg angle at the grating. Depending on the instantaneous modulation depth of the density grating, a fraction ($\sim 0.01\%$) of the interrogation beam is scattered into a coherent signal beam which is detected by a photomultiplier tube and recorded for data analysis. Figure 1a-f show examples of such signals. The trace in figure 1a is a typical LITA signal originating purely from thermalization. The speed of sound is encoded in the frequency of the oscillations (Brillouin frequency, *i.e.*, the local speed of sound divided by the grating's fringe spacing) in the signal. If the gas composition is known, the temperature can be deduced. The signal decay is governed by the beam geometry and
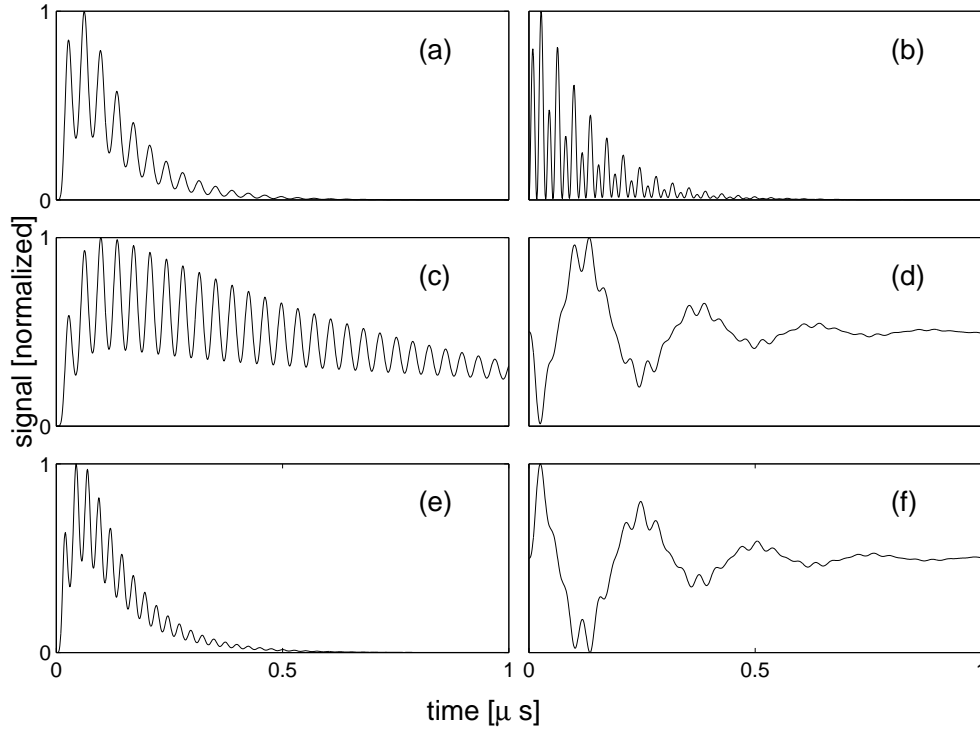
**Figure 1.** (a) Typical LITA signal from thermalization; (b) Comparable thermalization and electrostriction; (c) same as (a), but lower thermal diffusivity; (d) same as (a), but heterodyne detection and nonzero flow velocity; (e) same as (a), but higher speed of sound; (f) same as (d), but different phase shift between Brillouin and Doppler beating.

the thermal diffusivity. The thermal diffusivity is mostly a function of the fluid density which can be measured if the $D_T$-$\rho$-dependence is known. Compared to figure 1a, the signal in figure 1c corresponds to a fluid with lower thermal diffusivity but otherwise identical properties. The only difference between figure 1a and figure 1e is the higher speed of sound in figure 1e. Electrostriction causes oscillations at twice the Brillouin frequency. While the presence of either contribution depends on the composition of the fluid, the relative importance of these two effects, the ratio $\gamma_U$, if both are observed, is proportional to the concentration of a resonantly excited (thermalization) trace species within the non-resonantly excited (electrostriction) fluid [11]. Figure 1b shows a signal with comparable contributions from electrostriction and thermalization.

The density grating is convected with the surrounding fluid which results in a Doppler shift of the signal beam relative to the interrogation beam. This Doppler shift can be made visible by superimposing the signal beam with a reference beam at the original frequency. The Doppler shift then appears as additional frequency component in the signal (figure 1d, f). This detection approach is called heterodyne detection (vs. homodyne detection without reference beam). The introduction of a fixed frequency shift into the reference beam, *e.g.* by using a Bragg cell, has been suggested to remove the sign ambiguity of the velocity measurements and improve accuracy for low flow velocities [8]. The Doppler frequency is then modified by an amount equal to the

frequency shift. In the absence of such a frequency shift, the ratio of the Doppler shift to the Brillouin frequency is the flow Mach number. LITA velocimetry with a homodyne detection setup requires an offset between the excitation laser beams' focus and the interrogation beam. The time-of-flight of the inscribed grating is then measured, similar to the laser-two-focus (L2F) approach [12]. But instead of a "hot-spot", a grating structure is convected with the fluid, thereby allowing simultaneous measurements of the other quantities.

Single-shot LITA measurements consume only in the order of 1 $\mu$s. The density perturbations are less than 1% of the mean density. The errors are less than 1% (typically 0.1%) for the speed of sound, 1% (typically 0.25%) for the flow velocity, 5% for the concentration, and 10% for the thermal diffusivity. Data rates are only limited by the laser repetition rate where pulse energies typically have to be greater than 10 mJ. The signal beam can be filtered by wavelength as well as spatially, making LITA insensitive to flow luminosity. Possible applications include combustion [13] and hypersonic flow diagnostics.

## 3. Data Analysis Considerations

Several data analysis methods have been employed ranging from least-square fits of a physical [1] or generic [14] model to the data, over simple frequency decomposition techniques, to neural network implementations [15]. If only the speed of sound and the flow velocity are of interest, then a data analysis technique based on a frequency decomposition is the method of choice for its simplicity, efficiency, and numerical robustness. To extract information from the LITA signals which is not encoded as a frequency component, a more general technique has to be used. While the neural network approach satisfies the condition of generality, it will be cumbersome due to the training requirement of the neural network. A re-training is required with each change of the experimental parameters, which happens frequently in a research-type application. This leaves the fitting technique as only viable option if speed of sound, flow velocity, thermal diffusivity, and concentrations are to be measured simultaneously. The fitting technique can also be shown to be the most accurate data analysis method, provided that the mathematical model is an accurate representation of the physics [1]. The number of degrees of freedom of the problem increases with the number of simultaneous measurements. The dimensionality influences the convergence behavior and computational cost of the data analysis. The speed and robustness of the data analysis are of great importance for real-time applications.

Cummings *et al* [2] and Schlamp *et al* [15] derived a closed form analytical model for signals from LITA. Its parameters are the speed of sound, flow velocity, thermal diffusivity, electrostriction and thermalization magnitude. In addition, a number of experimental parameters are required that include the laser wavelengths, the laser beam crossing angle, the frequency shift (if any) of the reference beam with respect to the interrogation beam, and the Gaussian beam half-widths. The values of the experimental parameters are either known *a priori* or can be found in a calibration step where a measurement is performed in a fluid with known properties.

A random phase shift, $\tilde{\phi}$, between the Doppler and the Brillouin frequency beating (the only difference between the signals in figure 1d and f) complicates the fitting in the physical space because, due to its randomness, no good initial guess can be used for this parameter. This problem is avoided by performing the fitting using the spectra of the model and the data (also see section 4.8), i.e., the magnitude of the discrete

Fourier transform. This random phase shift also means that, if averaging is desired to improve the signal-to-noise ratio, the averaging has to be performed in the frequency domain (only for heterodyne detection). Otherwise, the LITA signals in a sample will cancel each other out. A second complication is that the signal depends on the ratios of thermalization and electrostriction magnitudes to the (known) intensity of the reference beam. In the limit where the reference beam is much stronger than the signals from either electrostriction or thermalization, only the ratio $\gamma_U$ of the thermalization to the electrostriction magnitudes comes to bear [15]. This is easily achieved experimentally by adjusting the intensity of the reference beam accordingly to operate in this limit, while not saturating the detector. Only in this limit and only for low concentrations of the resonantly excited species is $\gamma_U$ proportional to the concentrations.

These simplifications leave one with a four-dimensional domain $\mathcal{A}$ spanned by the four fitting parameters $(c_s, u_y, D_T, \gamma_U)$ with coordinates $(i, j, k, l)$, and a LITA signal $\underline{L}(t, i, j, k, l)$ on the point $(i, j, k, l)$ being a vector with $N$ points, where $N$ is the number of time-discretized data points within the signal. Then the least-squares error with respect to the measured LITA signal $\underline{L}^*(t)$ on the signal point $x(i, j, k, l)$ in $\mathcal{A}$ is

$$E(i, j, k, l) = \sum_{t=0}^{N} \left( \underline{L}^*(t) - \underline{L}(t, i, j, k, l) \right)^2 . \tag{1}$$

The fitting algorithm has to find the $(i, j, k, l)$ such as to minimize $E$ globally.

The problem of global optimization is encountered in many areas of the applied sciences and no single algorithm exists which combines the requirements for convergence to the *g*lobal minimum within *f*inite time. Commonly, the Levenberg-Marquardt scheme [16–18] is used, which belongs to the class of deterministic techniques, *i.e.*, it converges in finite time but not necessarily to the global minimum. It is a combination of the inverse Hessian technique (multi-dimensional Newton method) and the method of steepest descent and requires initial guesses for all parameters. Unfortunately, with increasing dimensionality the scheme becomes not only slower but also the convergence behavior deteriorates if the initial guesses are not "sufficiently close" to the global minimum. The algorithm does not converge at all in some instances or converges to obvious erroneous (local) minima of $E$. It is required that the error surface is smooth such that

$$\nabla E = \vec{0}, \tag{2}$$

where the gradient denotes differenciation with respect to the fitting parameters, is satisfied at a minimum. The success rate for the fitting routine depends on the "closeness" of the initial guesses from the global minimum and on the topology of the error surface (figure 2), *i.e.*, on the particular application. The structure of the error surface for the fitting procedure is investigated in the following section in order to quantify the requirements for the initial guesses to ensure convergence to the global minimum.

## 4. Numerical study

### 4.1. 4-dimensional error surface

The complexity of the theoretical model does not allow for an analytic analysis. One has to resort hence to a numerical study of the problem. Each combination

of parameters has its own four-dimensional error surface and it is impossible to study every possible combination. But it is expected that the topology of the error surface does not change qualitatively for a wide range of parameters. Therefore, some "typical" values are chosen for the speed of sound (350 m/s, approximately the value for atmospheric air), the flow velocity (50 m/s), the thermal diffusivity ($2 \times 10^{-5}$ m$^2$/s, corresponding to atmospheric air), and the thermalization-to-electrostriction ratio $\gamma_U$ (1, corresponding to equal contributions from thermalization and electrostriction). This condition corresponds to point labeled "$A$" in table 1. The experimental parameters were also chosen to reflect typical setups. 532 nm was used as excitation laser wavelength (frequency-doubled Nd:YAG laser), 488 nm for the interrogation laser wavelength (Argon-ion lasers), and 1.5° for the excitation laser beam crossing angle. Furthermore, a frequency shift of 10 MHz between the interrogation beam and the reference beam was assumed. A sampling time of 2 $\mu$s and a sampling rate of 256 MHz were assumed, resulting in 512 data point in each signal, allowing the use of the Fast-Fourier Transform algorithms.

Using these values in the theoretical model of Schlamp *et al* [15], a reference LITA signal spectrum (magnitude of Fourier transform) was calculated. Then, additional signal spectra were computed while changing the input parameters. The sum-of-squares difference between each spectrum and the reference spectrum was evaluated. Before calculating the spectra, each signal was normalized to a positive peak value of unity. This ensures that only the shape of the signal but not the absolute signal amplitude, which can exhibit a sizeable amount of variation within experiments, is used to determine the parameters. It is expected that noise also has an influence on the topology of the error surface. For this purpose, varying amplitudes of Gaussian noise were added to the reference signal (*i.e.*, before calculating the spectrum) and the procedure was repeated.

Figure 2 shows all six cross-sections of the four-dimensional error surface around the reference point $A$, *i.e.*, a point corresponding to air at atmospheric conditions and a flow velocity of 50 m/s. Red colors correspond to large deviations between the spectra, i.e., high values of the sum-of-squares difference $E$, while blue colors represent good agreement. The global minimum is located in the center of the dark blue region in each of the planes, as indicated by the white cross-hair. Note that for this figure, the theoretical model was used to calculate a signal for these conditions, *i.e.*, no noise is considered. The error at the global minimum is therefore zero. Many local minima are visible, particularly in the $c_s - u_y$-plane. The error surfaces for the other parameter combinations listed in table 1 are qualitatively the same as the one for point $A$ shown in figure 2 [20].

The ridge lines in the error surface in the $c_s - u_y$-plane correspond to situation where the Brillouin frequency is $n$ ($n$ being an integer) times or $1/n$ times the Doppler frequency. If the reference beam is not frequency shifted from the interrogation beam, then these line are lines of constant Mach number and the lines pass through the origin. In the present case (with a frequency shift), the Mach number changes along the lines, but all lines pass the axis $c_s = 0$ at a common point, where the Brillouin frequency equals the frequency shift. In particular, the most prominent line represents the case where the Brillouin and Doppler frequency are identical. A similar periodicity is visible as well in the other cross-sections involving the speed of sound (top right and center left on figure 2). The other views are less structured.

The thick white lines in figure 2 mark the boundary between regions within which a Levenberg-Marquardt algorithm, using the respective values as initial guesses for the
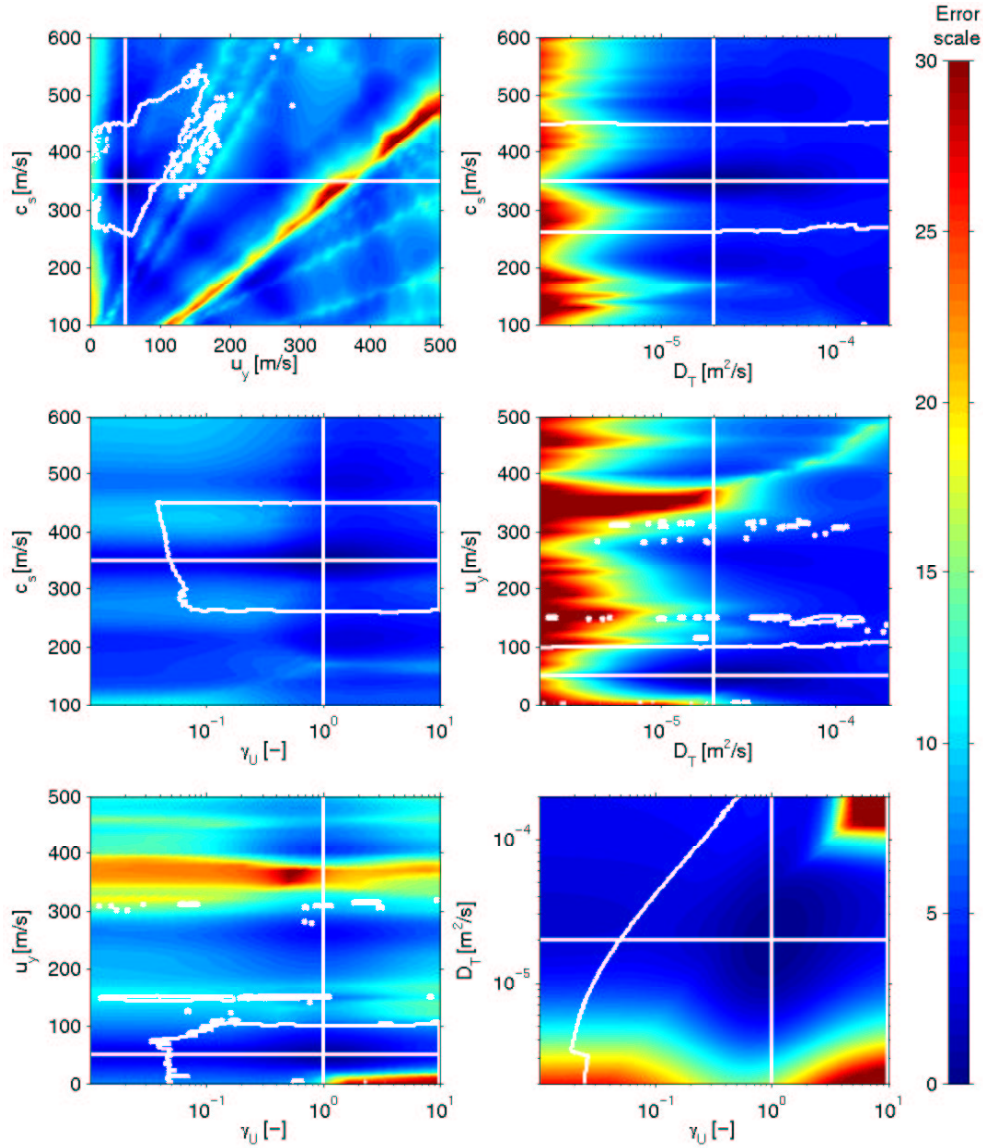
**Figure 2.** Six cross-sections of the error surface going through the point $(c_s, u_y, D_T, \gamma_U) = (350m/s, 50m/s, 2 \cdot 10^{-5}cm^2/s, 1)$. The global minimum is at the crossing of the white cross-hair. If initial guesses are taken from within the region inside the thick white lines, the Levenberg-Marquardt algorithm converges to the global minimum (compare with lower right plot in figure 8).

parameters, convergence to the global minimum. This feature is explained in more detail in section 4.5 and section 4.6.
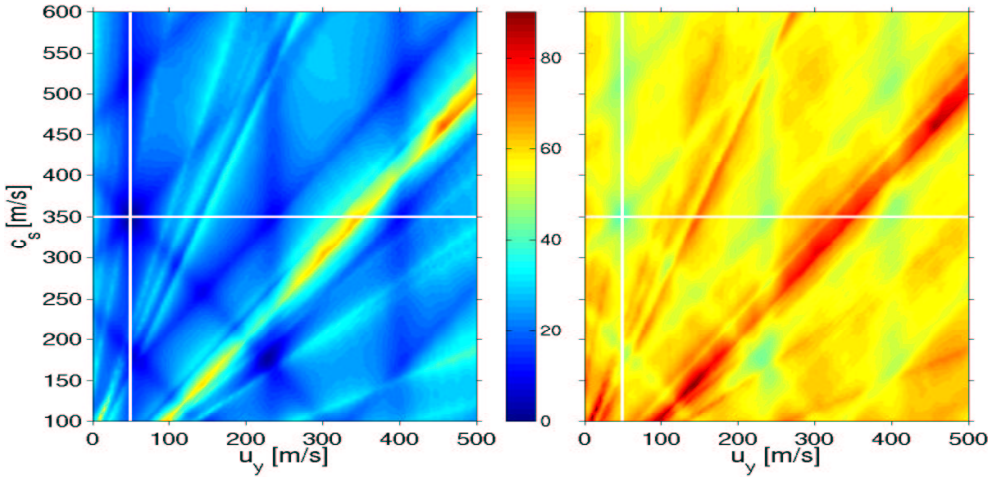
**Figure 3.** Change of error surface in the presence of noise. Left: no noise; right: SNR=3. SNR is based on standard deviation of Gaussian noise to peak signal amplitude.

### 4.2. Error surface with noise

The left half of figure 3 shows the the $(u_y - c_s)$-plane of the error surface without noise in the reference signal (same as top left of figure 2). The right plot is the error surface if noise is added to the reference signal. The signal-to-noise ratio (SNR) based on the standard deviation of the Gaussian noise and the peak signal amplitude is 3, which can be considered to be very noisy. Typical SNRs in experiments are one order of magnitude higher [19]. Due to the noise, the total error level is shifted toward higher values for $E$. Despite the high noise levels, the topology of the error surface appears to change only quantitatively. The noise adds more fine structure to the error surface.

### 4.3. Convergence neighborhood

In a second study, a total of eleven points in the parameter space are chosen as a representative sample. Their respective parameter values are shown in the left half of table 1. The four-dimensional error surface is then searched for local minima around each of these points. To limit the computational cost, the search is performed at a certain resolution for each of the parameters. This means that it is possible that additional local minima exist, which are not detected. But if this were the case, then these undetected minima have only a small neighborhood of convergence so that they can be neglected for practical applications. The local minimum closest (as measured by (3)) can be seen as a characteristic length scale for how critical the choice of the initial guesses of the fitting parameters is.

The initial guesses for the Levenberg-Marquardt scheme have to be within a neighborhood of the global minimum. A characteristic allowable deviation can be defined using the distance between the global minimum and the closest local minimum:

$$r_{char} = \left[ \left( \frac{c_s - c_s^*}{c_s^*} \right)^2 + \left( \frac{u_y - u_y^*}{u_y^*} \right)^2 + \left( \log \frac{D_T}{D_T^*} \right)^2 \right]$$

**Table 1.** Points out of 4-dimensional parameter space whose neighborhoods were examined for local minima. The correct values for the parameters are shown in the left half. The location of the closest (as measured by (3)) detected local minimum of the error surface are shown on the right. The characteristic distance $r_{char}$ is given in the very right column.

| Label | global minimum | | | | closest local minimum | | | | |
|---|---|---|---|---|---|---|---|---|---|
| | $c_s^*$ [m/s] | $u_y^*$ [m/s] | $D_T^*$ [m²/s] | $\gamma_U^*$ [-] | $c_s$ [m/s] | $u_y$ [m/s] | $D_T$ [m²/s] | $\gamma_U$ [-] | $r_{char}$ [%] |
| A | 350 | 50 | 2e-5 | 1.00 | 490 | 50 | 2.83e-5 | 1.58 | 47 |
| B | 200 | 50 | 2e-5 | 1.00 | 189 | 60 | 1.74e-5 | 1.23 | 23 |
| C | 500 | 50 | 2e-5 | 1.00 | 360 | 50 | 2.52e-5 | 1.58 | 36 |
| D | 350 | 150 | 2e-5 | 1.00 | 349 | 149 | 2.14e-5 | 1.15 | 7 |
| E | 350 | 350 | 2e-5 | 1.00 | 392 | 331 | 2.14e-5 | 0.87 | 15 |
| F | 350 | 450 | 2e-5 | 1.00 | 250 | 340 | 6.32e-5 | 0.63 | 66 |
| G | 350 | 50 | 1e-4 | 1.00 | 350 | 50 | 1.07e-4 | 1.07 | 4 |
| H | 350 | 50 | 4e-6 | 1.00 | 520 | 50 | 6.32e-6 | 1.58 | 56 |
| J | 350 | 50 | 2e-5 | 0.02 | 380 | 80 | 5.02e-5 | 0.06 | 88 |
| K | 350 | 50 | 2e-5 | 0.10 | 230 | 30 | 5.02e-5 | 0.10 | 66 |
| L | 350 | 50 | 2e-5 | 5.00 | 180 | 50 | 2.24e-5 | 6.31 | 50 |

$$+ \left( \log \frac{\gamma_U}{\gamma_U^*} \right)^2 + \left( \frac{\tilde{\phi} - \tilde{\phi}^*}{2\pi} \right)^2 \Bigg]^{1/2} , \tag{3}$$

where the stared quantities denote the values of the global minimum and the unstared values the location of the closest local minimum. The distance for the thermal diffusivity and for $\gamma_U$ are taken in a logarithmic sense, which reflects their physical behavior (spanning several orders of magnitude). The error of the initial guess for the phase shift $\tilde{\phi}$ is irrelevant if the entire analysis is performed on the power spectra of the signals, but important in the time domain (section 4.8 and section 4.9). This length scale does not provide information as to how large the convergence neighborhood around this local minimum is or as to how many local minima there are within a certain distance, both of which has a significant influence on the convergence behavior. If the local minimum has a small neighborhood of convergence and if there are only few local minima at a distance comparable to $r_{char}$, then the fitting scheme will usually converge if the distance of the initial guesses from the global minimum is greater than the $r_{char}$ and only if they are within an isolated region within the four-dimensional space around the closest local minimum will it converge to this local minimum.

The values for the speed of sound, flow velocity, thermal diffusivity, and thermalization-to-electrostriction ratio for the closest local minimum are given in the right half of table 1. The column on the very right shows their distance $r_{char}$ from the global minimum. Typical values for $r_{char}$ are around and above 50%, but are very small for some combinations of parameters. For points $E$ and $G$, a poor behavior was expected. For point $E$, the Mach number is unity and hence the Brillouin frequency and the Doppler frequency are almost identical (but not the same due to the frequency shift). A large value for the thermal diffusivity was chosen for point $G$, which results in a very quick decay of the signal, reducing the amount of usable information it contains. The proximity of the local minimum for point $D$, however, is not easily explained and indicates that there exist combinations of parameters for which the choice of the initial values has to be very good. A closer examination around point $A$ reveals that a total

**Table 2.** Local minima with $r < 1$ around parameter combination $A$. The searched region is $c_s = 100 \ldots 600 \text{m/s}$, $u_y = 0 \ldots 500$ m/s, $D_T = 2 \cdot 10^{-6} \ldots 2 \cdot 10^{-4}$ m$^2$/s, and $\gamma_U = 0.01 \cdots 10$. The region is searched with a resolution of 51 equally spaced steps for $c_s$ and $u_y$, 41 logarithmically spaced steps for $D_T$, and 31 logarithmically spaced steps for $\gamma_U$.

| $c_s$ m/s | $u_y$ m/s | $D_T$ $10^{-5}$ m$^2$/s | $\gamma_U$ - | $r$ % |
|---|---|---|---|---|
| 490 | 50 | 2.83 | 1.58 | 47 |
| 210 | 50 | 3.17 | 1.58 | 49 |
| 490 | 50 | 5.02 | 1.00 | 57 |
| 480 | 40 | 5.02 | 1.00 | 58 |
| 210 | 50 | 3.99 | 2.00 | 58 |
| 500 | 60 | 3.99 | 2.00 | 64 |
| 210 | 60 | 5.64 | 1.26 | 64 |
| 190 | 70 | 2.83 | 1.58 | 66 |
| 480 | 40 | 6.32 | 1.26 | 66 |
| 230 | 30 | 5.02 | 0.79 | 67 |
| 200 | 50 | 7.10 | 1.58 | 73 |
| 210 | 60 | 7.10 | 1.58 | 74 |
| 200 | 70 | 3.99 | 2.51 | 77 |
| 470 | 30 | 7.96 | 1.26 | 80 |
| 200 | 50 | 8.93 | 2.00 | 83 |
| 570 | 60 | 4.48 | 2.51 | 85 |
| 130 | 20 | 2.24 | 1.26 | 88 |
| 180 | 80 | 5.02 | 0.63 | 89 |
| 450 | 20 | 8.93 | 1.00 | 93 |

of 12 local minima exist within a range of $r < 75\%$ (see table 2). A refined search in a smaller region did not find additional local minima.

### 4.4. Error and uncertainty

Noise will also influence the accuracy and uncertainty of the data analysis by shifting the global minimum away from its nominal position. To quantify this effect, the parameter values in the first row of table 1 (point $A$) were used to calculate a LITA signal, which was normalized to a positive peak value of unity. Before taking the power spectrum, 100 different Gaussian random samples of noise were then added to this signal. A least-squares fit using a subspace trust region algorithm based on the interior reflective Newton method [21, 22] is used as implemented in Matlab (©The MathWorks) to fit the theoretical model to the spectrum of the noisy signal. The initial guesses ($c_s + 10$ m/s, $u_y + 10$ m/s, $1.5 * D_T$, $\gamma_U/1.5$, corresponding to $r = 60\%$) were chosen close to the expected minimum because only the shift of the global minimum was of interest. Cases in which the fitting did not converge were not considered in the subsequent analysis.

The error (as measured by the average shift of the global minimum) and uncertainty (as measured by the standard deviation of the shift) for the four parameters are shown in figure 4a and b, respectively. The uncertainty decreases with increasing signal-to-noise ratio with a power-law dependence. The absolute uncertainties for the velocity and the speed of sound are equal. For subsonic flows, the relative error for the velocity is therefore higher than for the sound speed measurements. Noise can also lead to a shift of the mean of the location of the

global minimum. But the error is approximately two orders of magnitude below the uncertainty at equal signal-to-noise ratio for each of the parameters. For a signal-
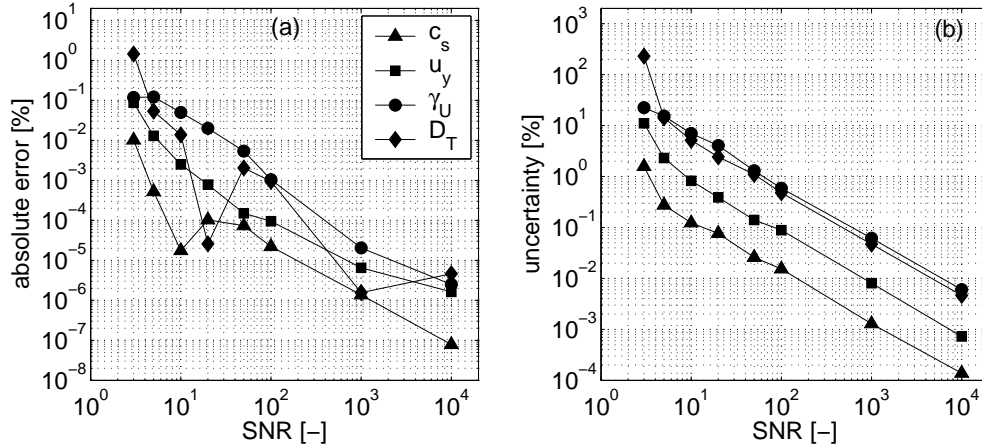


**Figure 4.** Absolute values of relative errors (a, left) and uncertainties (b, right) in % as a function of the signal-to-noise ratio.
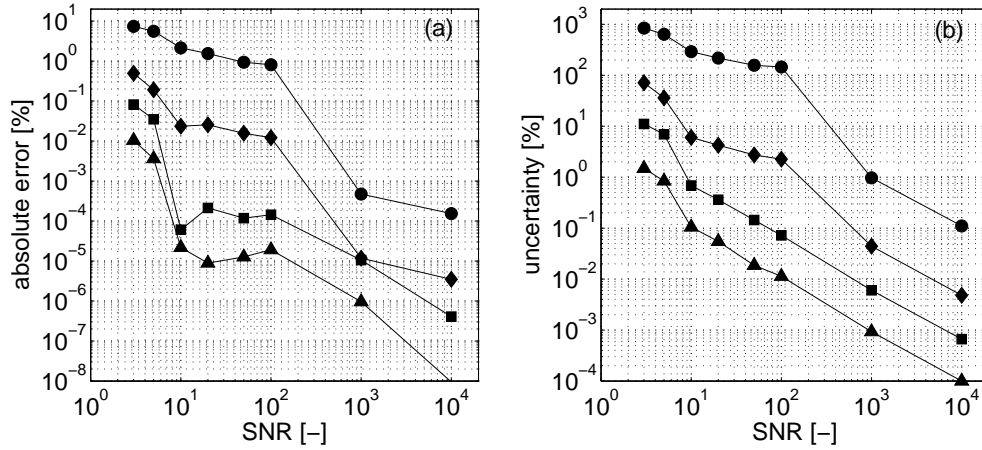


**Figure 5.** Same as figure 4, but for point 08.

to-noise ratio of 50, which is typical for experiments [19], the uncertainty is 0.025% for the speed of sound, 0.15% for the flow velocity, and slightly above 1% for the thermal diffusivity and for $\gamma_U$. The absolute uncertainties for the speed of sound and the flow velocities are identical 0.2 m/s. This value is probably only a function of the sampling rate, *i.e.*, the number of data points for each signal. These uncertainties are only due to the data analysis and are in addition to any uncertainty within the experiment. Figure 5 gives the same data for the parameter combination $J$. Only the value for $\gamma_U$ is different for this case, but the uncertainties for all four parameters are approximately three to four times higher than for point $A$, they decrease with the same slope, however. The uncertainty for $\gamma_U$ itself is larger than 100% for SNRs up to 100, which is only possible if the fitting algorithm converges to a value more than twice as large as the correct value. This is plausible, since the correct value for this

parameter of $\gamma_U = 0.02$ is such that thermalization has only a negligible effect on the total signal, which reduces the accuracy and certainty of the technique. The same effect has been observed experimentally for the case of negligible electrostriction [11]. Mathematically, the error surface is flatter than for the case before, so that comparable noise levels can more easily shift and add minima.

### 4.5. Convergence behavior vs. r

Figure 6a shows how the probability of convergence to the global minimum depends on the quality of the initial guesses and on the SNR. The Levenberg-Marquardt algorithm was applied to signals with parameter combinations $A$ and $J$ with different noise levels added and with random initial guesses for a total of $108,000$ fits for each parameter combination. The initial guesses, number of function calculations (section 4.7), and fitted parameters were recorded. Convergence to global minimum was defined such that the error is less than $0.5\%$ for the speed of sound, less than $5\%$ for the flow velocity, and less than $25\%$ for the thermal diffusivity and the ratio of thermalization to electrostriction. These thresholds correspond to approximately twice the uncertainties at a SNR of 5 (figure 4b). This is independent of the fitting routine's convergence criterion, *i.e.*, where it stops, although convergence to some minimum within a given number of iterations is an additional condition for successful convergence to the global minimum. These thresholds will also result in some false negative results for very low signal-to-noise ratios, but experimentally only SNRs greater than 20 are of interest and increasing the thresholds to accommodate all SNR would result in false positives for intermediate and high SNRs.

The convergence success rate does not depend on the SNR. The lower success rates for SNR$\leq 5$ are due to false negatives because of the set thresholds. For $SNR \geq 20$ and $r \leq 0.2$, all of the fits are successful. This ratio drops to $80\%$ for $r \leq 0.3$. The first value for $r$ correspond to approximately $r_{char}/2$. This threshold depends in general on the fitting algorithm and its settings, such as the initial step size, *etc.*, but in this case is comparable in size with the value for $r_{char}$.

Figure 7a shows the same information as figure 6a but for the reference point $J$ (table 1). Since this point exhibits higher uncertainties at comparable SNRs, the thresholds for the successful convergence condition are adjusted to $2\%$ for the sound speed, $20\%$ for the flow velocity, and $100\%$ for the thermal diffusivity. No threshold is set for $\gamma_U$. The region of guaranteed convergence is slightly stretched to $r = 0.3$ and drops to $80\%$ for $r = 0.4$. For this reference point, the closest local minimum is at $r_{crit} = 88\%$, almost twice the critical radius of point $J$.

Table 3 shows the cross-correlation coefficients between the probability of successful convergence to the global optimum (for all SNRs) and the individual deviations of the initial guesses from the correct values, *i.e.*,

$$r_{c_s} = \left| \frac{c_s - c_s^*}{c_s^*} \right| \quad r_{u_y} = \left| \frac{u_y - u_y^*}{u_r^*} \right|$$

$$r_{D_T} = \left| \log \frac{D_T}{D_T^*} \right| \quad r_{\gamma_U} = \left| \log \frac{\gamma_U}{\gamma_U^*} \right| \tag{4}$$

A zero correlation coefficient would indicate no influence of the initial guess on the probability of convergence success. Negative values mean, that the better the initial guesses are the more likely a convergence to the global optimum is. The initial guess for the speed of sound is more strongly correlated than the other parameters, showing
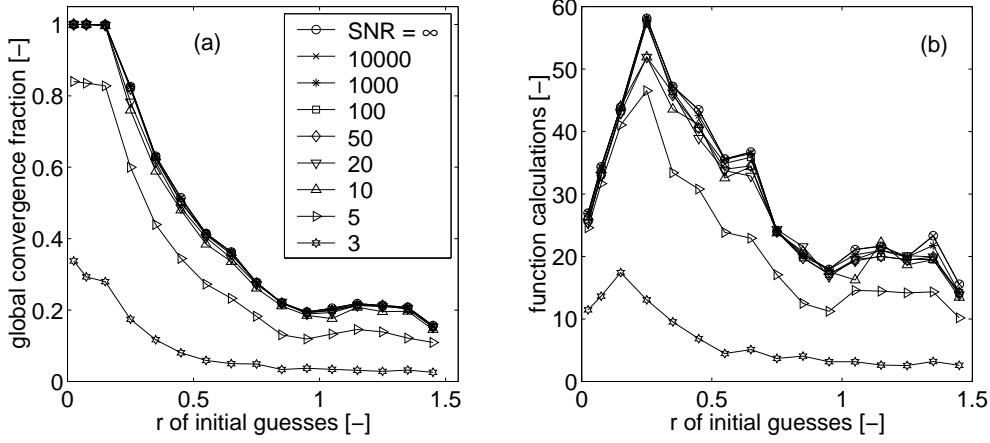
**Figure 6.** (a) Fraction of signals that converge to the global minimum with the Levenberg-Marquardt algorithm vs. "closeness" of initial guesses for different signal-to-noise ratios. (b) Number of necessary function calculations for convergence to global minimum. $r_{char} = 0.47$ for reference point $A$.
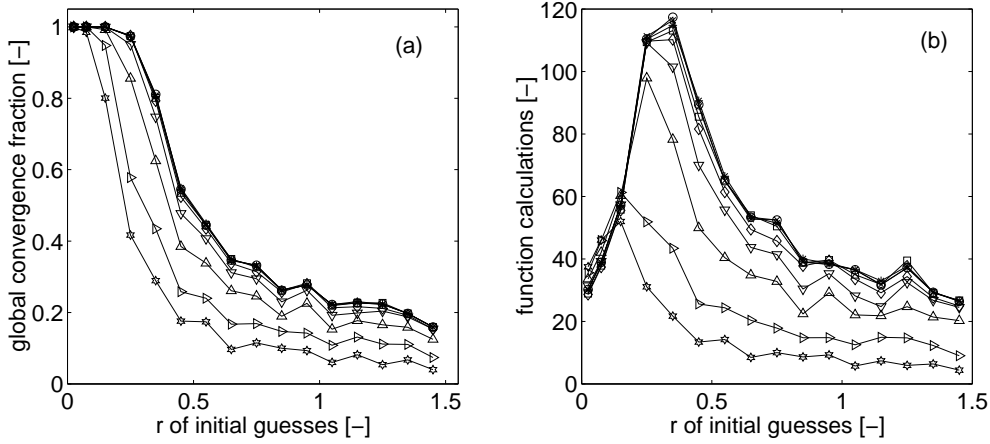


**Figure 7.** Same as Fig. 6, but for reference point $J$ with $r_{char} = 0.88$.

**Table 3.** Correlation coefficients between global convergence success and distance of individual distances of parameters from global optimum as well as the total distance $r$.

| reference point | cross-correlation coefficients w.r.t. | | | | |
|---|---|---|---|---|---|
| | $r_{c_s}$ | $r_{u_y}$ | $r_{D_T}$ | $r_{\gamma_U}$ | $r$ |
| 00 | $-0.7403$ | $-0.4436$ | $-0.3807$ | $-0.3869$ | $-0.5485$ |
| 08 | $-0.8011$ | $-0.5365$ | $-0.4372$ | $-0.4354$ | $-0.6136$ |

that the initial guess for this parameter is more critical than the others. The cross-correlation coefficients for $u_y$, $D_T$, and $\gamma_U$ are approximately equal.
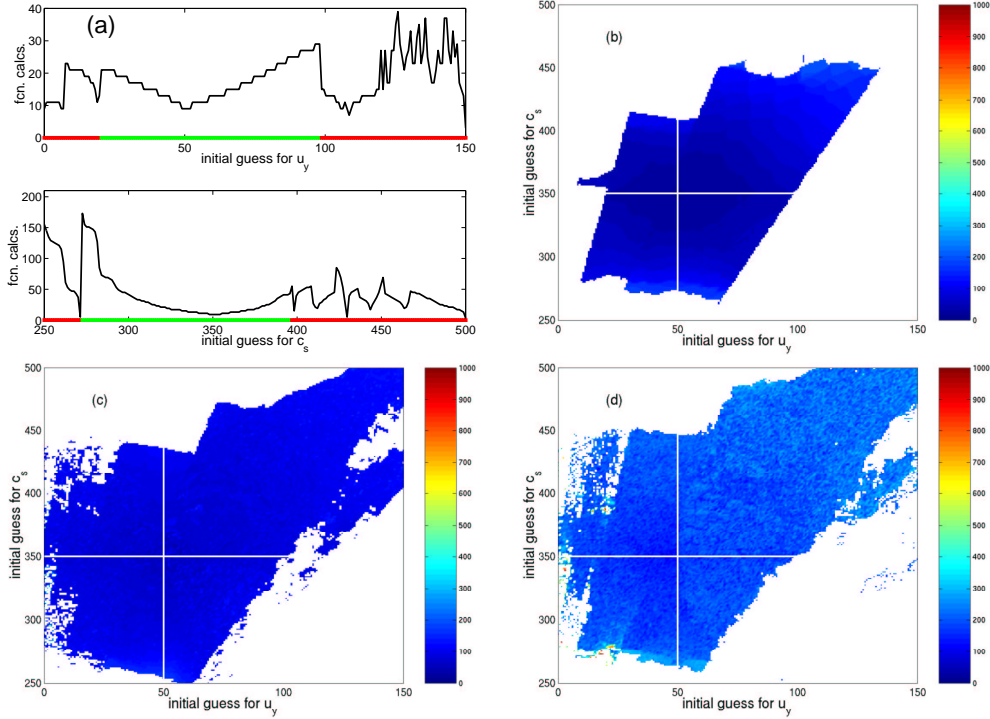
**Figure 8.** Dependence of convergence behavior on the dimensionality of the parameter space. (top left): Convergence neighborhood if the flow velocity (top half) or the speed of sound (bottom half) is the only fitting parameter and all other parameters are set to (and held at) the correct values. If the initial guess falls within the green region, then the fitting algorithm converges to the global optimum at $u_y^* = 50$ m/s or at $c_s^* = 350$ m/s, respectively; Plotted is also the number of required function calculations using the theoretical model. (top right): Convergence neighborhood if flow velocity and speed of sound are both fitted for. Colors correspond to the number of required function calculations (for clarity, only plotted inside of convergence neighborhood). (bottom left): Convergence neighborhood and computational cost if speed of sound, flow velocity, and thermal diffusivity are fitting parameters. (bottom right): All four parameters are fitted.

## 4.6. Convergence behavior vs. number of parameters

Figure 8a-d shows the convergence neighborhood in the $c_s - u_y$-plane for different numbers of fitting parameters around point $A$ and for SNR= $\infty$. In the top plot of figure 8, only the speed of sound is assumed unknown while all other parameters are held at the correct values. The green bar shows the region of initial guesses that lead to convergence to the correct speed of sound, while initial guesses in the region marked red converge to other (local) minima. A maximum number of 250 iterations and 1,000 function calculations were allowed in the Levenberg-Marquardt scheme. Furthermore, the same convergence criteria are used as in section 4.4. Also plotted is the number of required function calculations. The bottom half shows the corresponding plot when only the flow velocity is assumed as unknown. For both cases, the computational cost is least when the initial guesses are close to the global minimum and increase continuously with the distance of the initial guesses from there. Note the difference

in computational cost (as measured by the number of function calculations) between the two parameters. Figure 8b shows the case where the speed of sound and the flow velocity are both assumed unknown. The colors correspond to the number of function calculations. Regions in which the algorithm converged to local minima are left white for clarity. In figure 8c a third parameter, the thermal diffusivity, is also allowed to float in the fitting. The initial guess, however, is set to the correct value. In figure 8d then, all four parameters are fitted, but the initial guesses for $D_T$ and $\gamma_U$ are the respective correct values. The same color scale is chosen for figure 8b-d. Note the increase in computational cost from figure 8a to figure 8c with increasing dimensionality (number of unknowns) of the fitting, which has two reasons: Firstly, the local derivatives of the error surface with respect to each fitted parameter are calculated numerically at each iteration. Hence, the number of required function calculations only for the derivative computation is proportional to the dimensionality of the problem. Secondly, the total number of function calculations is the number of function calculations per iteration times the number of iterations and, while not shown in figure 8, the number of iterations also increases with increasing number of fitting parameters, resulting in a faster-than-linear growth of the computational cost. In all cases it is observed that the computational cost tends to increase with increasing distance of the initial guesses from the global minimum, indicated by the white cross-hairs.

The colored regions in figure 8b-d and the regions marked green in figure 8a are the convergence neighborhoods of the error surface in this particular plane and using this particular algorithm. The convergence neighborhoods for the other cross-sections corresponding to the case shown in figure 8d are plotted as thick white lines in figure 2. The exact boundaries depend on the optimization algorithm employed but are expected to be similar to those shown in figure 8. In figure 8c &d, isolated regions exist that do converge to the global minimum surrounded by regions that do not (only in this plane). Thus, the fitting must have taken a path circumventing any white regions by using the extended dimensionality of the parameter space. This is not possible for the case in figure 8b, where no such additional dimensions. There is, however, a small isolated patch visible above the top edge of the boundary. The white gap must have been crossed by a sufficiently large step size in the Levenberg-Marquardt algorithm.

The additional dimensions can also host additional local minima and so the convergence neighborhood does not necessarily increase in area with an increasing number of degrees of freedom, *e.g.*, the area of the "peninsula" on the right side of the convergence neighborhood's boundary in figure 8c, but which was not present in figure 8b, has shrunk in size in figure 8d. The boundaries are oriented along the ridge lines of the error surface visible in figure 2. Figure 8 demonstrates that the characteristic length $r_{char}$ can only be taken as such, because the convergence neighborhoods are nowhere near circular (using $r$ as metric).

While it seems from figure 8b-d that the region of convergence increases with the number of fitting parameters and that the conditions for the initial guesses are hence less stringent, this is not true. Note that the out-of-plane initial guesses are the correct values in figure 8c and d. In practice, this is not the case. From the results in section 4.5 it can be seen that the initial guesses for each parameter can only approximately 15%, if one assumes that all initial guesses have the same error. But if, like in the case of figure 8d, two initial guesses are exact, the two remaining initial guesses can have an error of 21% each. And if three of the four initial guesses are correct, then the fourth one can have an error of 30%. Latter value agrees well

with the results in figure 8 for the initial guess for the speed of sound. The vertical extent of the convergence region at $u_y = 50$ m/s is approximately 200 m/s, *i.e.*, $\pm 28\%$. The span in the horizontal direction at $c_s = 350$ m/s does not agree with this value, but is close to $\pm 100\%$ for the initial guess of the flow velocity. In fact, as can be seen from the convergence boundaries in figure 2, if two of the initial guesses are exact (the speed of sound not being one of them), then the speed of sound limits the convergence neighborhood the most. In comparison, the initial guesses for the thermal diffusivity and for $\gamma_U$ can be off by an order of magnitude. This agrees with the finding of the increased correlation between the error of the sound speed initial guess and the convergence rate compared with the other parameters (table 3).

## *4.7. Computational cost*

Using the same procedure and data as in section 4.4, figure 6b depicts the number of required function calculations (of the theoretical LITA model) for the cases where the fitting converged to the global minimum for point $A$ as a function of the initial guesses and the SNR. The absolute numbers depend on the details of the fitting scheme, but the dependence will behave similarly. The number of function calculations increases initially with increasing $r$, which is the intuitively expected dependence. The number drops, however, again for $r > 0.35$, which could indicate a different weighing of the Newton to the inverse Hessian scheme within the Levenberg-Marquardt algorithm for these cases. This behavior and the absolute numbers are independent of the SNR, with the exception of the lowest SNR.

Figure 7b shows the computational cost for point $J$ as reference. For this combination of parameters, almost twice as many function calculations are required, but the the behavior is qualitatively identical to figure 6b. The slower convergence is another indication for smaller gradients, *i.e.*, a flatter error surface. This matches the observation of higher uncertainties than for point $A$ at comparable noise levels (see figure 4b and figure 5b).

## *4.8. Time vs. frequency domain analysis*

Figure 9 shows results comparable to those in figure 8d. Here, however, the data analysis was performed using the signals in time domain rather than working with their spectra. As mentioned in section 3, a random phase shift, $\tilde{\phi}$ influences the signal shapes (figure 1d and f) and has to be taken as an additional parameter. The randomness of $\tilde{\phi} = 0 \ldots 2\pi$ makes it impossible to give good initial guesses in the fitting. Figure 9a shows the theoretical case where $\tilde{\phi}$ is assumed known and held constant in the fitting. The fitting is thus performed on a four-dimensional parameter space, which corresponds to the case shown in figure 8d. The color scaling is chosen identical to the one in figure 8b-d. Compared to these earlier results, the convergence neighborhood is smaller, but the number of function calculations is significantly lower. This case of known $\tilde{\phi}$ is a pure theoretical case and cannot be achieved experimentally. Slightly more realistically are the results shown in figure 9b. $\tilde{\phi}$ is added to the list of fitting parameters, but the initial guess is assumed to be the correct value. The convergence neighborhood for this case is larger than in figure 9a, but still smaller than in figure 8d. The number of required function calculations has increased dramatically within most of the convergence neighborhood compared with both, figure 8d and figure 9a. The parameter space in now 5-dimensional.
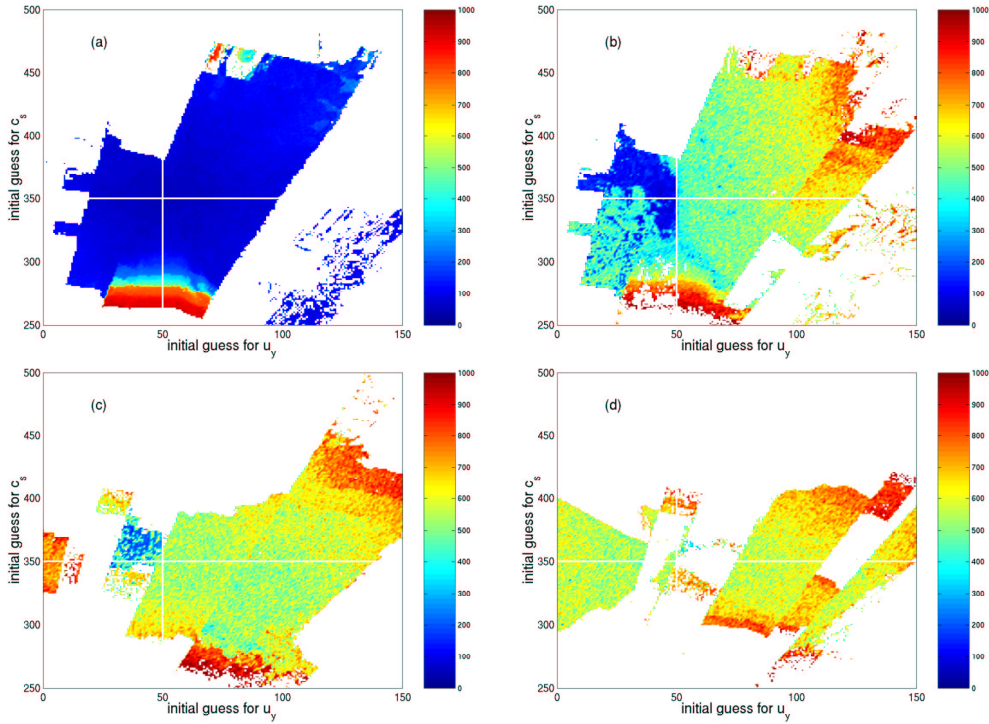
**Figure 9.** Convergence neighborhood if data analysis is performed in time instead of frequency domain; compare with figure 8d. (a): The random phase shift $\tilde{\phi}$ between Doppler and Brillouin oscillations is assumed known and held constant; (b): The random phase shift is a fifth fitting parameter, but with correct value as initial guess; (c): initial guess for $\tilde{\phi}$ is off by $\pi/2$; (d): initial guess for $\tilde{\phi}$ is off by $\pi$.

The results shown in figure 9c and d show the effect of an initial guess for $\tilde{\phi}$ that is off by $\pi/2$ (figure 9c) and $\pi$ (figure 9d), respectively. For these cases, even initial guesses for the speed of sound and the flow velocity that are very close to the correct solution might not lead to convergence to the global minimum. Since $\tilde{\phi}$ is purely random from a range $0 \ldots 2\pi$, the initial guess is off by $\pi/2$ in average and figure 9c can be seen as representative for an experimental application. Figure 9d is a worst-case scenario with respect to the initial guess for the phase shift. Comparing the number of function calculations in figure 8 and 9b-d, the benefit of the frequency domain for the data analysis is evident. The additional computational cost for the fast Fourier transform at each function calculation is negligible compared to function calculation itself.

## 4.9. Two-step methods

Hart *et al.* [23] employ Prony's method to extract initial guesses for the speed of sound, the flow velocity and the phase shift from the signal in the time domain. These are subsequently used as initial guesses for a more accurate Levenberg-Marquardt algorithm. Figure 10 shows the convergence behavior of the Levenberg-Marquardt algorithm in the time and frequency domain for varying maximum errors of the initial
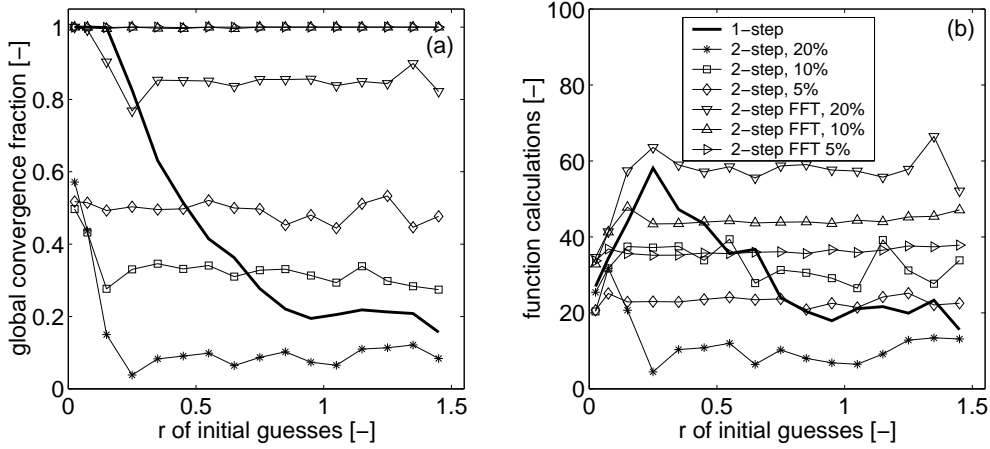
**Figure 10.** Convergence behavior (a, left) and computational cost (b, right) if better initial guesses are obtained for $c_s$, $u_y$, and $\tilde{\phi}$ by data preprocessing. For comparison, the bold solid line represents the result from figure 6 without noise. It is assumed that the maximum error of the intial guesses for each of the three parameters is 20, 10, and 5%. The other two parameters can deviate further. Results are shown for employing the fitting routine to signals in the time domain and to the power spectra of the signals (data denoted by "FFT").

guesses for the speed of sound, the flow velocity, and the phase shift (for time domain only). The isgnals are considered noiseless (infinite signal-to-noise ratio). The same global convergence criterion is chosen as in figure 6.

The improved initial guesses do not improve the convergence behavior sufficiently if the fitting is performed in the time domain. Even if the initial guesses are within 5% of the correct value, only half of the fits converge to the global minimum. When fitting the power spectra, the same data preprocessing ensures convergence if the maximum estimation error is 10%. Still 90% of the fits are successfull for a maximum estimation error of 20%. The success rate does not depend on the choice for the remaining initial guesses, which shows that the initial guesses for the speed of sound and the flow velocity are more critical than initial values for the thermal diffusivity and $\gamma_U$.

Compared with figure 6, the computational cost is higher for larger values of $r$. This is due to the fact that $r$ is now largely determined by the thermal diffusivity and $\gamma_U$. As can be seen from figure 2, the error surface is flatter in the direction of these parameters. Hence, if the fit does converge for a given $r$, it converges faster if the error terms for $D_T$ and $\gamma_U$ are small than if the total error is due to errors in those two parameters.

## 5. Summary and Conclusions

When laser-induced thermal acoustics is to be applied for the simultaneous measurements of the speed of sound, flow velocity, thermal diffusivity, and a species concentration simultaneously, special consideration has to be given to the data analysis. It has been shown that the data analysis is more stable and more efficient in the frequency than in the time domain. This is due to a random phase shift between the Brillouin and the Doppler frequency components in the signal. For the

same reason, averaging over multiple laser shots, if desired, has to be performed by averaging the spectra and not the signals themselves.

The topology of the error surface, the convergence neighborhood, and the computational cost of the data analysis do not depend significantly on the noise levels in the signals. Signal noise does, however, increase the uncertainty contributed to the data analysis. The exact amount depends on the local steepness of the error surface.

Convergence of the Levenberg-Marquardt algorithm is also a function of the closeness of the initial guesses to the global minimum. The distance of the closest local minimum (as measured by (3)) has been defined as characteristic length scale. The convergence success rate correlates with this length scale. To ensure convergence to the global minimum, the initial guesses have to be within a certain fraction (one third to one half) of this characteristic length scale around the global minimum. Of the four parameters, the initial guess for the speed of sound is most critical. The maximum deviation of the initial guesses as measured by (3) is in the order of 30% for all four parameters combined, *i.e.*, each initial guess has to be within approximately 15% of the correct value. This requires an accordingly precise prior knowledge of the result or a visual inspection of the result of the fitting. The shape of the convergence neighborhoods, however, is not symmetrical around the global minimum. If the fitting technique converges to a local minimum instead of the global minimum, the signals for the respective parameters will look quite distinct and hence a visual inspection of the fitting result reveals it.

Proper convergence can be ensured by obtaining improved initial guesses for some parameters by means of data preprocessing, e.g. by using Prony's method to extract initial guesses for the speed of sound and the flow velocity. Even if an initial guess for the random phase shift is available, performing the fitting an the signals' spectra, on which the random phase shift has no influence, yields more reliable convergence. In particular, if the speed of sound and the tehrmal diffusivity are known to within 10%, then the Levenberg-Marquardt scheme converges regardless of the initial guesses for the thermal diffusivity and the thermalization-to-electrostriction ratio.

Only a small number of points were examined in the previous section. An examination of the entire parameter space is not possible. But it is expected that the qualitative behavior and the topology of the error surface do not change except for special cases, *e.g.*, when the Brillouin and Doppler frequencies are identical. The results will also depend slightly on the fitting algorithm, its implementation, and the parameter settings of the algorithm.

## References

[1] Cummings E B 1995 *Laser-Induced Thermal Acoustics* (Ph.D. thesis, California Institute of Technology).
[2] Cummings E B, Leyva I A and Hornung H G 1995 Laser-induced thermal acoustic (LITA) signals from finite beams *Appl. Opt.* **34**(18) p 3290-302.
[3] Cummings E B 1994 Laser-induced thermal acoustics (LITA): simple accurate gas measurements *Opt. Lett.* **19** p 1361-3.
[4] Butenhoff T J 1995 Measurement of the thermal-diffusivity and speed of sound of hydrothermal solutions via the laser-induced grating technique, *Intl. J. of Thermophys.* **16**(1) p 1-9.
[5] Hemmerling B, Kozlov D N and Stampanoni-Panariello A 1999 *Measurement of gas flow velocities by electrostrictive laser-induced gratings* (Book of abstracts, XVIII European CARS Workshop: CARS and related gas-phase diagnostics, C.R. ENEA, Frascati, Italy, March 21-23).
[6] Schlamp S 2000 *Laser-Induced Thermal Acoustic Velocimetry* (Ph.D. thesis, California Institute of Technology).

[7] Stampanoni-Panariello A, Hemmerling B and Hubschmid W 1998 Temperature measurements in gases using laser-induced electrostrictive gratings *Appl. Phys. B* **67**(1) p 125-30.

[8] Schlamp S, Cummings E B and Sobota Th H 2000 LITA velocimetry using heterodyne detection *Opt. Lett.* **25**(4) p 224-6.

[9] Schlamp S and Allen-Bradley E 2000 Homodyne detection laser-induced thermal acoustic velocimetry *AIAA Paper* 2000-0376.

[10] Walker D J W, Williams R B and Ewart P 1998 Thermal grating velocimetry *Opt. Lett.* **23**(16) p 1316-8.

[11] Schlamp S and Sobota Th H 2000 Measuring concentrations with laser-induced thermalization and electrostriction gratings *submitted to Experiments in Fluids*.

[12] Kost F and Kapteijn C 1997 Application of laser-two-focus velocimetry to transonic turbine flows (7th Intl. Conf. on "Laser Anemometry – Advances and Applications", University of Karlsruhe, Germany).

[13] Brown M S and Roberts W L 1999 Single-point thermometry in high-pressure sooting, premixed combustion environments *J. of Propulsion and Power* **15**(1) p 119-27.

[14] Hart R C, Balla R J and Herring G C 1999 Nonresonant referenced laser-induced thermal acoustic thermometry in air *Appl. Opt.* **38**(3) p 577-84.

[15] Schlamp S, Hornung H G and Cummings E B 2000 Neural network data analysis for laser-induced thermal acoustics *Meas. Sci. Technol.* **11**(6) p 784-94.

[16] Press W H, Flannery B P, Teukolsky S A and Vetterling W T 1986 *Numerical Recipes* (Cambridge University Press, Cambridge/MA).

[17] Levenberg K 1944 A method for the solution of certain problems in least squares *Quarterly Applied Math. 2* p 164-8.

[18] Marquardt D 1963 An algorithm for least squares estimation of nonlinear parameters *SIAM Journal Applied Math.* **11** p 431-41.

[19] Schlamp S, Hornung H G, Sobota Th H and Cummings E B 2000 Accuracy and uncertainty of single-shot, nonresonant laser-induced thermal acoustics *Appl. Opt.* **39**(30) p 5477-81.

[20] Schmid L 2001 *Error Analysis for Laser-Induced Thermal Acoustics* (Diploma thesis, Institute of Fluid Dynamics, ETH Zürich).

[21] Coleman T F and Li Y 1996 An interior, trust region approach for nonlinear minimization subject to bounds *SIAM Journal on Optimization* **6** p 418-45.

[22] Coleman T F and Li Y 1994 On the convergence of reflective Newton methods for large-scale nonlinear minimization subject to bounds *Mathematical Programming* **67**(2) p 189-224.

[23] Hart R C, Balla R J and Herring G C 2001 Simultaneous velocimetry and thermometry of air by use of nonresonant heterodyned laser-induced thermal acoustics *Appl. Opt.* **40**(6) p 965-8.